Composites: Part A 76 (2015) 224–232

Contents lists available at ScienceDirect

Composites: Part A

journal homepage: www.elsevier.com/locate/compositesa

Damage resistance and damage tolerance of hybrid carbon-glass laminates

Andrew T. Rhead *, Shi Hua, Richard Butler

Department of Mechanical Engineering, University of Bath, Bath BA2 7AY, United Kingdom

ARTICLE INFO

Article history:
Received 8 January 2015
Received in revised form 21 April 2015
Accepted 1 June 2015
Available online 8 June 2015

Keywords:
A. Hybrid
B. Damage tolerance
B. Impact behaviour
B. Strength

ABSTRACT

The influence of impact energy and stacking sequence on the damage resistance and Compression After Impact (CAI) strength of Carbon and Glass Fibre Reinforced Plastic (CFRP and GFRP respectively) hybrid laminates is investigated. CAI tests demonstrate that, in comparison to fully CFRP laminates, hybrid laminates show increases in structural efficiency of up to 51% for laminates subject to a 12J impact and 41% for those subject to an 18J impact. Laminates displaying the highest stresses at failure are those that exploit stacking sequences and GFRP content to prevent delaminations from forming close to the outer surface of the laminate during impact. This favourable damage morphology inhibits both sublaminate-buckling-driven delamination propagation and anti-symmetric laminate buckling failures.

1. Introduction

In order to meet emission and structural efficiency targets it is inevitable that the next generation of commercial aircraft will show a significant and increasing reliance on the favourable strength and stiffness properties of Carbon Fibre Reinforced Plastics (CFRP). However, a number of factors are preventing CFRP from being utilised to its full potential, amongst which Barely Visible Impact Damage (BVID) is of particular significance. BVID, which may be caused by dropped tools and impact of small runway debris, leaves surface indentations which are too small to be seen on routine aircraft inspections yet can cause considerable internal damage. Under compressive loading such damage can propagate and cause considerable overall strength reduction [1–3].

The HiPerDuct program [4,5] has explored the use of hybrid carbon/glass laminates to significantly increase ductility of laminates. This was noted to be a consequence of Glass Fibre Reinforced Plastic (GFRP) plies maintaining laminate integrity at high strain levels by bridging broken CFRP fibres. This paper aims to determine whether the addition of GFRP layers to CFRP laminates can have an enhancing effect on Compression After Impact (CAI) strength.

Previous examples of hybridization of laminates aimed at enhancing resistance to BVID formation and/or the CAI properties of laminates include adding aramid (Kevlar) interlayers to CFRP laminates [6–8] and GLAss-REinforced Fibre Metal Laminates (GLARE) [9,10]. In particular, it is reported [11] that laminates with non-CFRP surface layers have damage "in the surface plies" and delaminations "between the surface layers and the CFRP underneath". This indicates that the use of non-CFRP surface plies could offer protection from damage to a central core of load carrying fibres leading to higher strains to failure. Similarly, the residual flexural strength of impacted laminates with aramid fibre outer plies was found to be higher than for laminates with CFRP plies outermost (provided the impact did not cause penetration i.e. those where BVID occurred). In other work, a number of hybrid laminates [12], with a single stacking sequence through which the ply material was varied, were impacted and then tested to failure under tension, flexure and shear loading. Those coupons with aramid fibre outer layers were shown to have significantly improved residual strengths for a comparatively small loss in pristine compressive strength. The increased residual strengths were attributed to the high strain energy to failure exhibited by aramid plies in comparison to CFRP plies [12]. GFRP plies have similarly high strain energy to failure and it has been demonstrated [13] that the failure strength of GFRP (but not CFRP) plies increases considerably with increasing rates of applied strain, e.g. those rates of strain seen in impact events. Thus GFRP plies may confer improved damage resistance. GFRP layers have previously been added to CFRP helicopter blades [14] where their progressive, non-catastrophic failure mechanism (established in load deflection tests) was seen as an advantage for compressive failures where damage was not a factor. Here it is considered this above mechanism may lead to increased strength in a CAI regime. An additional factor in the choice of GFRP as the hybridisation material is that

* Corresponding author. Tel.: +44 (0) 1225 386373.
E-mail address: A.T.Rhead@bath.ac.uk (A.T. Rhead).

http://dx.doi.org/10.1016/j.compositesa.2015.06.001
1359-835X/

GFRP plies have a considerable cost advantage over CFRP and aramid plies.

In this paper, the influence of stacking sequence and both position and number of glass layers on hybrid laminate damage resistance and CAI strength is investigated. A range of laminates, are subject to out-of-plane impacts at 12J or 18J (Section 3) and then to CAI testing (Section 4). CFRP only laminates with a stacking sequence that has previously [2] been identified as being damage tolerant are used as comparative baselines. Discussion of results from Ultrasonic C-scan, X-ray Computed Tomography (CT) and Digital Image Correlation (DIC) systems in Section 5 shows that the favourable damage morphology exhibited by the impacted hybrid laminates is key to their improved CAI strength and structural efficiency.

2. Laminate manufacture and stacking sequence selection

The effect of GFRP layers on damage tolerance is to be studied through their introduction at various through thickness positions. Both hybrid CFRP/GFRP and CFRP only coupons (dimensions shown in Fig. 1) were manufactured from carbon (HTA/913C) and glass (GE5/913) pre-preg layers. Material properties [15,16] are given in Table 1 and stacking sequences and laminate properties given in Table 2. Laminate ID's are also defined in Table 2; the first letter denotes either a CFRP only (C) laminate or a hybrid laminate (H). The second letter denotes whether the stacking sequence is damage tolerant [2] (D), blocked (B) or homogenised (H). The following number determines whether GFRP layers are present in the outer and inner blocks (±45) or inner block only (0). Subscripts 'c' and 'g' differentiate between coupons by indicating whether, within each block, a CFRP or GFRP ply occurs first in the stack and hence nearer the coupon surface.

Note that residual thermal stresses usually prevent blocking of more than four plies of the same orientation together. However, the dissimilar stiffnesses of the 0° CFRP and GFRP plies appears to have overcome this issue as no evidence of any thermally induced delamination or intra-ply cracking was found. Based on laminate areal mass, $M_L = t_c\ \rho_c + t_g\ \rho_g$, (where $t_c(t_g)$ is total thickness of CFRP(GFRP) and $\rho_c(\rho_g)$ is CFRP(GFRP) density), hybrid laminates were nominally 8.2% or 12.2% heavier than the purely CFRP laminates, see Table 2.

Laminate stacking sequences were chosen in order to maintain a similar value of axial modulus, E_{xx}, whilst allowing GFRP content and layer positions to be varied, see Table 2. The CD and HB laminates employ a damage tolerant stacking sequence that has been shown [2] to offer improved residual strength. Placement of ±45° plies towards the outer surfaces of these laminates protects a central core of load carrying 0° plies from involvement in sublaminate buckling and hence delamination propagation [2]. Furthermore, ±45° surface plies offer high sublaminate buckling resistance (delaying the formation of this key failure mechanism), and low axial stiffness, limiting the accumulation of strain energy in the outermost sublaminates and thus increasing the strain required to propagate delaminations. This effect is magnified for the $HB45_g$ sequence which has low modulus GFRP ±45° outer layers and a greater proportion of central CFRP 0° plies increasing laminate axial modulus. Use of external ±45° also improves full laminate buckling performance. The homogeneous stacking sequence, HH, is widely used in the aerospace industry as it allows ply-drops to be easily incorporated thereby ensuring surface and ply continuity across thickness variations. A comparison of HB

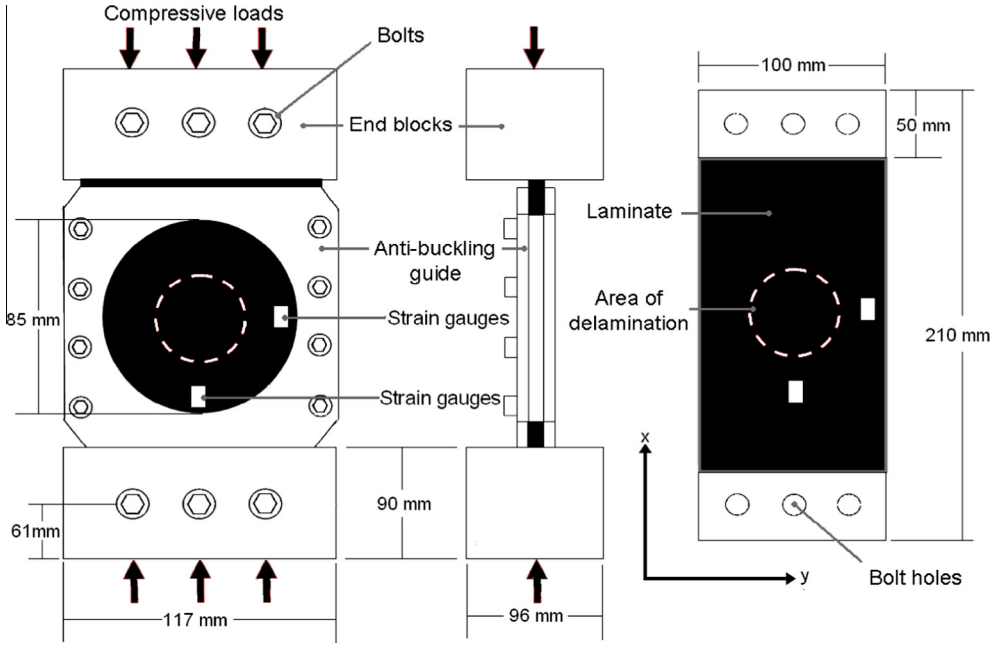

Fig. 1. Experimental CAI set-up and coupon details. (For interpretation of the references to colour in this figure legend, the reader is referred to the web version of this article.)

Table 1
Material properties [15,16] (t is cured layer thickness and ρ is material density).

Material	E_{11} (GPa)	E_{22} (GPa)	G_{12} (GPa)	ν_{12}	t (mm)	ρ (kg/m^3)	G_{IC} (J/m^2)	G_{IIC} (J/m^2)
GE5/913 (glass)	43.9	15.4	4.29	0.28	0.142	1930	225–300	1500–1700
HTA/913C (carbon)	135.0	18.5	4.97	0.29	0.134	1545	225–300	1500–1700

Table 2
Stacking sequence, nominal laminate thickness T, GFRP content, laminate areal mass ρ_L, theoretical axial modulus E_{xx}, and overall bending stiffness in the longitudinal (D_{11}) and transverse (D_{22}) directions. Note CD, HB and HH refer to CFRP only Damage tolerant, Hybrid Blocked and Homogenised Hybrid laminates respectively.

Laminate ID	(c = HTA/913C, g = GE5/913)	T (mm)	GFRP layers (%)	M_L (kg/m^2)	E_{xx} (GPa)	D_{11} (kN mm)	D_{22} (kN mm)
CD	$[(\pm45_c)_4/(0_c/90_c)_4]_S$	4.29	0	6.62	55	340	322
HB45$_c$	$[\pm45_c/45_c/(\mp45_g)/-45_c/\pm45_c/(0_c/0_g)_4]_S$	4.38	37.5	7.43	55	335	262
HB45$_g$	$[(\pm45_g)_2/(\pm45_c)_2/((0_c)_3/0_g)_2]_S$	4.38	37.5	7.43	65	291	199
HB0$_c$	$[(\pm45_c)_4/(0_c/0_g)_4]_S$	4.35	25	7.16	55	366	293
HB0$_g$	$[(\pm45_c)_4/(0_g/0_c)_4]_S$	4.35	25	7.16	55	350	293
HH	$[45_c/-45_c/0_c/0_g]_{4S}$	4.35	25	7.16	55	455	237

and HH results allows the relative effects of GFRP content and stacking sequence on laminate strength to be assessed.

The CD and HB stacking sequences are not intended to prevent delamination formation during impact. Delamination is a necessary process for impact energy absorption. Preventing formation of delaminations will lead to increased matrix cracking and fibre failure and thus reduced strength [17]. These laminates are instead designed to contain delamination to the core of the laminate preventing or delaying the occurrence of sublaminate-buckling driven delamination propagation.

The placement of glass layers on the outer surface of the HB45$_g$ laminate increases the detectability of damage by improving impact damage visibility; a consequence of a change in the opacity of GFRP layers in the vicinity of matrix damage (delamination/intra-ply cracking). Better damage visibility leads to the BVID limit being defined by a lower energy impact and thus smaller delaminations, resulting in an improved CAI strength. However, aerospace structures are often painted and so it may be difficult to take of advantage of the above in-service.

3. Impact testing and results

3.1. Impact test method

Coupons were subjected to single 12J or 18J out-of-plane impacts at their (plan form) centre using an Instron Dynatup 9250 instrumented impact testing machine. A 16 mm diameter hemispherical impactor was used to impact coupons clamped over a 75 mm × 125 mm test window (the long edge being aligned parallel to the 0° fibre axis) as prescribed by ASTM standard D7136/D7136M-07 [18]. Coupon dimensions are given in Fig. 1. The extent of BVID following impact was measured using an Ultrasonic Sciences Ltd. C-scan system employing a high-resolution 35 MHz probe, see Figs. 2 and 3. In addition to the C-scan data, a Nikon H 225ST X-ray CT system was used to scan an HH coupon (subjected to a 14J impact) and an HB0$_g$ coupon (subjected to an 18J impact) see Fig. 4. The HH coupon was cut down to 40 mm × 60 mm to improve CT scan quality and hence no CAI test result is reported.

3.2. Impact results

To differentiate between different test results an additional impact energy term is added to the end of the laminate ID. Where tests have been repeated with the same impact energy, an ‘a’ or ‘b’ is also appended to the ID.

Fig. 5 shows: (a) load vs. time, (b) deflection vs. time and (c) impact energy vs. time impact histories for the CD-18Ja, HH-18J, HB45$_g$-18J, and HB45$_g$-18J coupons. For the first nine interfaces from the non-impact face, the diameter of circle with minimum area that contains the total delamination at that individual interface is given in Table 3. Diameters are based on analysis of C-scans of the impacted laminates, see Figs. 2 and 3. Through thickness positioning of delaminations is based on a combination of C-scan output, stacking sequence analysis and comparison with X-ray CT data where available, e.g. Fig. 4. Positioning of delaminations is accurate to the nearest interface. Note that the largest delamination for coupon CD-18Ja had a diameter of 41 mm and occurred at the 12th interface ($90_c/0_c$) from the non-impact face.

3.3. Discussion of impact results

Although Fig. 5(c) shows that all coupons received the same peak impact energy, peak forces (Fig. 5(a)) and peak displacements (Fig. 5(b)) differed considerably. The least stiff response to impact was shown by the HB0$_c$-18J and HB45$_g$-18J coupons. These laminates allowed the formation of a favourable structured hat-shaped damage morphology (see Fig. 4(c) and (d)); the HB45$_g$-18J showing less stiffness owing to its more flexible GFRP outer plies. The stiffest response to impact was shown by the CD-18J coupon. This is a consequence of the higher carbon fibre content and 90° plies (not present in other coupons) providing a mutually supportive quasi-isotropic fibre architecture. The next stiffest response was offered by the HH-18Ja coupon where a homogenised fibre architecture led to the formation of unstructured, multi-level damage, see Fig. 4(a) and (b).

Stacking sequence and in particular blocking of plies into either ($45_c/-45_c$) and ($0_c/0_g$) or ($45_c/-45_c$) and ($-45_g/45_g$) groups is correlated with both the distribution of delamination and the maximum delamination diameter, see Table 3. Ply blocking produces interfaces with sharp contrasts in dominant ply direction and abrupt changes in the direction of principal bending stiffness. These discontinuities result in large interlaminar stresses [19]. As the resin matrix type is the same for all plies (and fibre material on its own has a limited effect on fracture toughness) it is these discontinuities rather than differences in toughness between CFRP and GFRP (e.g. G_{IC} and G_{IIC}) that drive damage morphology.

Fig. 4(c) and (d) shows that under impact the HB0$_g$-18J coupon formed a single hat-shaped beam of $0_c/0_g$ layers below the impactor that became separated from the rest of the $0_c/0_g$ plies through intra-ply cracking. This hat-shaped beam subsequently forced the $(\pm45)_4$ block of layers adjacent to the non-impact face to peel away from the ($0_c/0_g$) block inducing large delaminations at their interface. This well-structured damage produced the largest delaminations (see Table 3) but led to favourable residual strength, see below. A comparison of damage distributions and through thickness position of the largest diameter delamination clearly demonstrates this mechanism is prevalent in other HB coupons, see Table 3. The consistency of damage distributions and positioning of the largest delamination near the interface separating blocks of dissimilar plies, indicates the insensitivity of this damage morphology to variation in impact energy. Conversely, in the CD laminates although the largest delamination size increases with impact energy, through-thickness distribution of delaminations is inconsistent, with the CD1-12J laminate developing more near surface delaminations than the CD-18J laminates. It is likely that this inconsistency is either driven by imperfections in the resin or fibres, or by a dynamic effect possibly linked to bend-twist coupling. In the HH coupons all even interfaces separate blocks of ($45_c/-45_c$) and ($0_c/0_g$) plies. This leads to multi-level delamination, with more evenly dispersed and smaller delaminations, contrast images in Fig. 4 and see Table 3. As for the

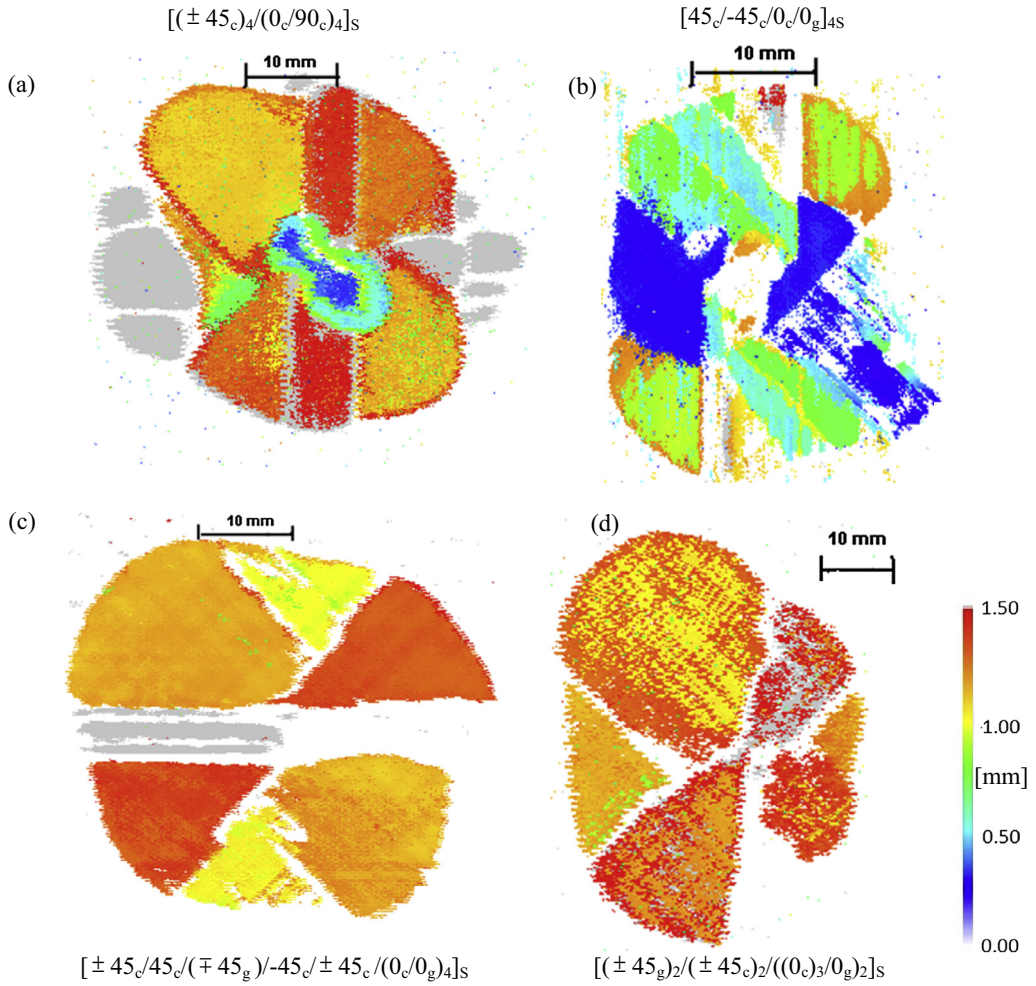

Fig. 2. C-scan images of delaminations caused by impact in (a) CD-18Ja, (b) HH-18J, (c) HB45$_c$-12J and (d) HB45$_g$-18J laminates. Delamination colouring indicates distance of delamination from the non-impact face and is consistent across images. In each scan the 0° fibre axis is vertical. (For interpretation of the references to colour in this figure legend, the reader is referred to the web version of this article.)

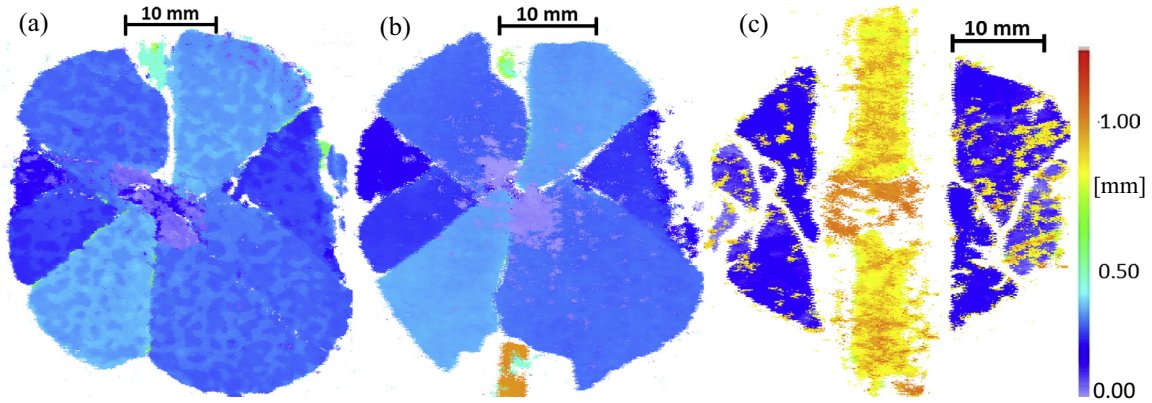

Fig. 3. C-scan images of the HB0$_g$-18J, [(± 45$_c$)$_4$/(0$_c$/0$_g$)$_4$]$_S$, from (a) the non-impact face following impact, (b) the non-impact face following compression after impact testing and (c) the impact face following compression after impact testing. Delamination colouring indicates distance of delamination from the non-impact face and is consistent across images. In each scan the 0° fibre axis is vertical. (For interpretation of the references to colour in this figure legend, the reader is referred to the web version of this article.)

CD laminates, distribution of delaminations is inconsistent with varying impact energy and thus maybe imperfection sensitive.

As anticipated, impact damage visibility and hence BVID detectability was improved by placing GFRP layers on the outside of the HB45$_g$ laminate. This was due to the formation of opaque through-thickness regions in the outer glass plies (particularly on the non-impact face) that were easily distinguished from the translucent intact glass regions. However, external aircraft surfaces are painted and thus this increased visibility will only apply to internal surfaces or to inspection of surfaces prior to painting. All other laminates received damage ostensibly below the BVID limit with no indication of fibre breakage and with dent depth discernible by touch or close visual inspection only.

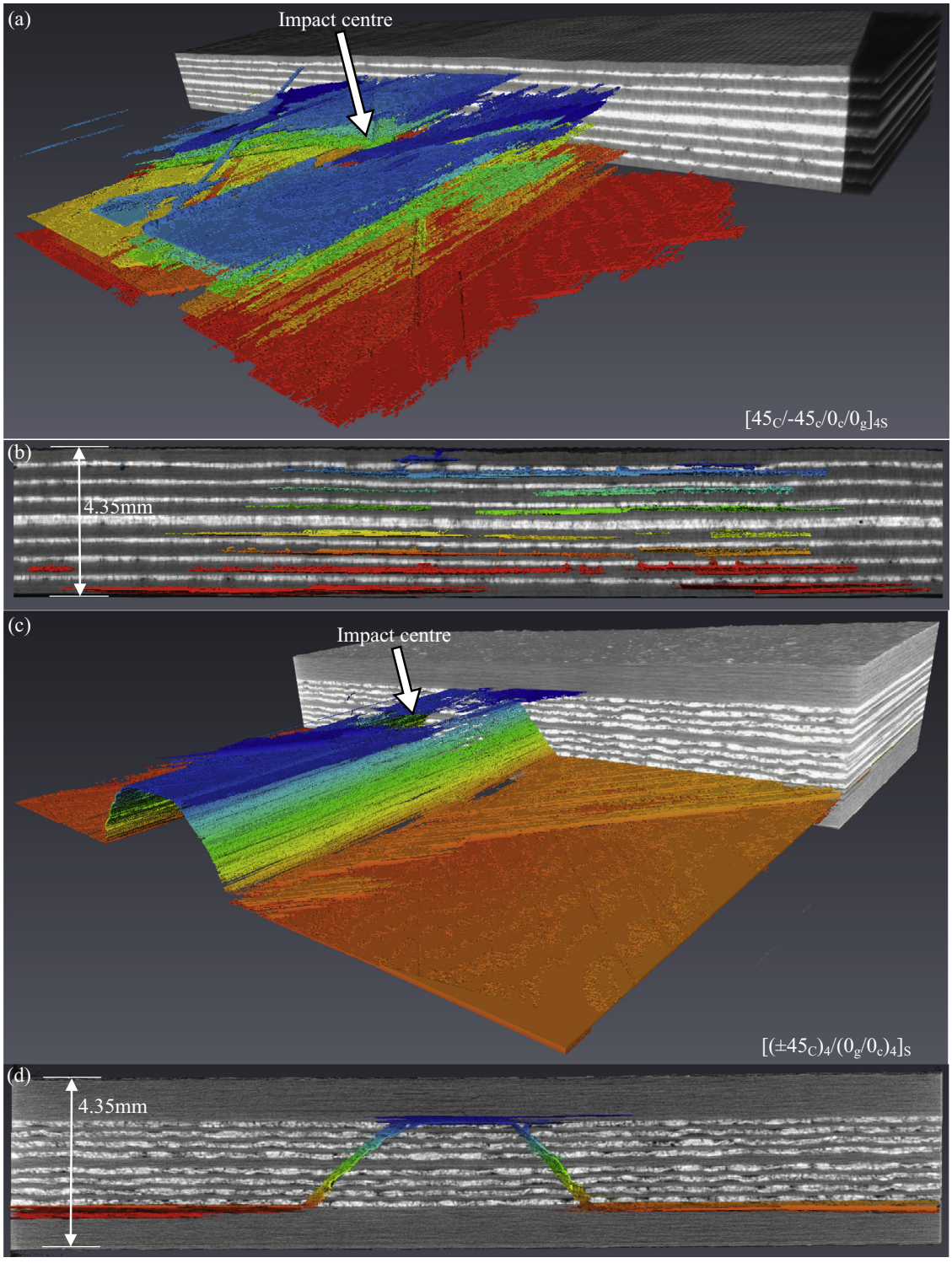

Fig. 4. X-ray CT cross-sections and 3D distributions of delaminations and intraply cracks following impact: (a and b) the HH-14J coupon, (c and d) the $HB0_g$-18J coupon. White layers are GFRP. Colours are indicative of delamination depth. Impact is to the top of the coupon. Scales are approximate. (For interpretation of the references to colour in this figure legend, the reader is referred to the web version of this article.)

4. Compression After Impact (CAI) testing and results

4.1. CAI test method

Following impact laminates were given aluminium end tabs and placed in a compression fixture with an integrated circular anti-buckling guide of internal diameter 85 mm (see Fig. 1). Axial compression was applied under displacement control at 0.1 mm/min until sublaminate-buckling-driven delamination propagation and/or overall failure occurred. In order to detect buckling modes and failure sequences the non-impact faces of the coupons, where delaminations are largest, were monitored using a Limess (Correlated Solutions) DIC system employing a stereo pair of Photron SA3 cameras. To ensure specimens were correctly aligned,

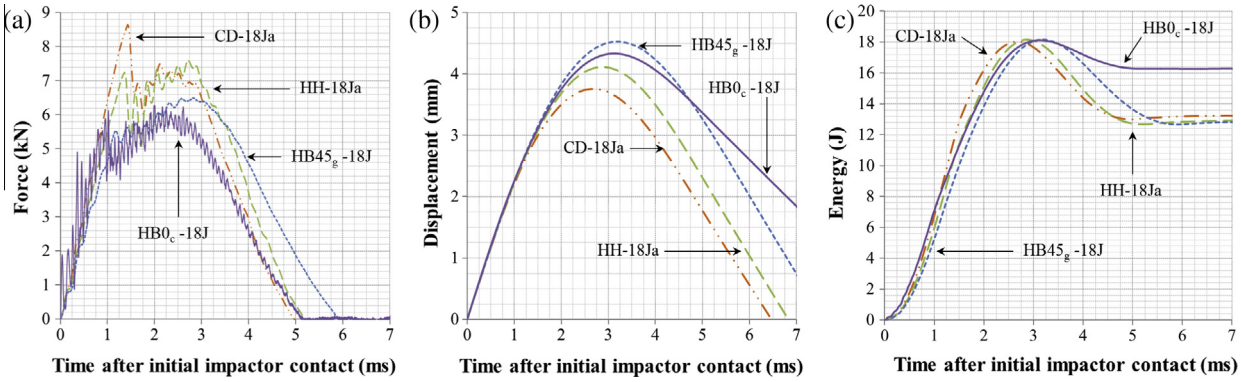

Fig. 5. Impact time history for the CD-18J, HH-18J, $HB0_g$-18J and $HB45_g$-18J coupons; (a) impactor displacement following initial contact vs. time, (b) force vs. time and (c) energy vs. time. (For interpretation of the references to colour in this figure legend, the reader is referred to the web version of this article.)

Table 3
Diameters of circles (in mm) containing delamination damage at individual ply interfaces as defined by C-scans of each coupon. Maximum diameters are given in bold. Patterned blocks represent ply angle (0° horizontal). GFRP layers are coloured green (online only). Note that the largest delamination in the CD-18Ja laminate is 41 mm and occurs at the 12th interface.

Laminate ID.	Ply number from back face									
	1	2	3	4	5	6	7	8	9	10
CD -12J	15	-	24	30	31	**36**	13	16	6	
CD -18Ja	-	16	-	-	-	-	20	-	-	
CD -18Jb	-	11	-	16	-	-	**44**	37	38	
HH -12J	12	26	-	-	20	**31**	29	-	-	
HH -18J	-	21	-	-	30	-	-	**34**	-	
$HB45_c$ -12J	-	-	-	-	42	**49**	45	-	-	
$HB45_g$ -12J	-	-	-	-	-	13	**57**	54	-	
$HB45_g$ -18J	-	-	-	-	-	50	**60**	57	-	
$HB0_c$ -12J	-	-	-	-	-	41	48	**50**	-	
$HB0_g$ -12J	-	-	-	-	54	-	**59**	50	-	
$HB0_g$ -18J	-	13	-	-	7	41	**48**	46	-	

"–" implies little or no delamination damage.

strains were recorded throughout the tests by two pairs of vertically aligned back-to-back strain gauges. See Fig. 1 for a schematic diagram of strain gauge placement.

4.2. CAI results

Table 4 gives stresses to failure and the failure mode (see Fig. 6) for each coupon with the exception of the $HB0_g$-12J and $HB0_g$-18J coupons for which testing was halted before failure. Failure stresses were calculated by dividing the corresponding loads by the nominal cross-sectional area for each laminate i.e. a coupon width of 100 mm multiplied by the laminate thickness T given in Table 2. Values in the final column of Table 4 represent a coupon structural efficiency calculated by dividing experimental stress to failure by laminate areal mass, see Table 1. Failure of the laminates occurred via a range of mechanisms determined from a combination of XRCT images (Fig. 4), DIC images (Fig. 6) and load vs. strain plots (Fig. 7). Despite the use of an anti-buckling guide during compression testing, DIC and strain gauge results indicated that all coupons underwent overall bending deformation. Strain gauge failure occurred before coupon failure in some tests. Average strain gauge readings at failure for these coupons were thus extrapolated (see Fig. 7(c) and (d)) based on laminate stiffness prior to gauge failure.

Table 4
Impact energy, buckling modes, initial propagation stress σ_{th} experimental failure stress σ_F and structural efficiency of coupons.

Laminate ID-impact energy	Buckling mode	σ_F Experimental failure stress (MPa)	σ_F/M_L (MN/kg)
CD-12J	Local (Sublaminate)	233	35.2
CD-18Ja	Overall (anti-symmetric)	235	35.5
CD-18Jb	Overall (anti-symmetric)	235	35.5
HH-12J	Local (sublaminate)	285	39.8
HH-18J	Local (sublaminate)	264	36.9
$HB45_c$-12J	Overall (symmetric)	342	46.1
$HB45_g$-12J	Overall (symmetric)	343	46.2
$HB45_g$-18J	Overall (symmetric)	313	42.1
$HB0_c$-12J	Overall (symmetric)	372	52.0
$HB0_g$-12J	Overall (symmetric)	>382[a]	>53.3
$HB0_g$-18J	Local (sublaminate)	>359[a]	>50.1

[a] Test was halted before final failure occurred to assess propagation of damage from the impact site.

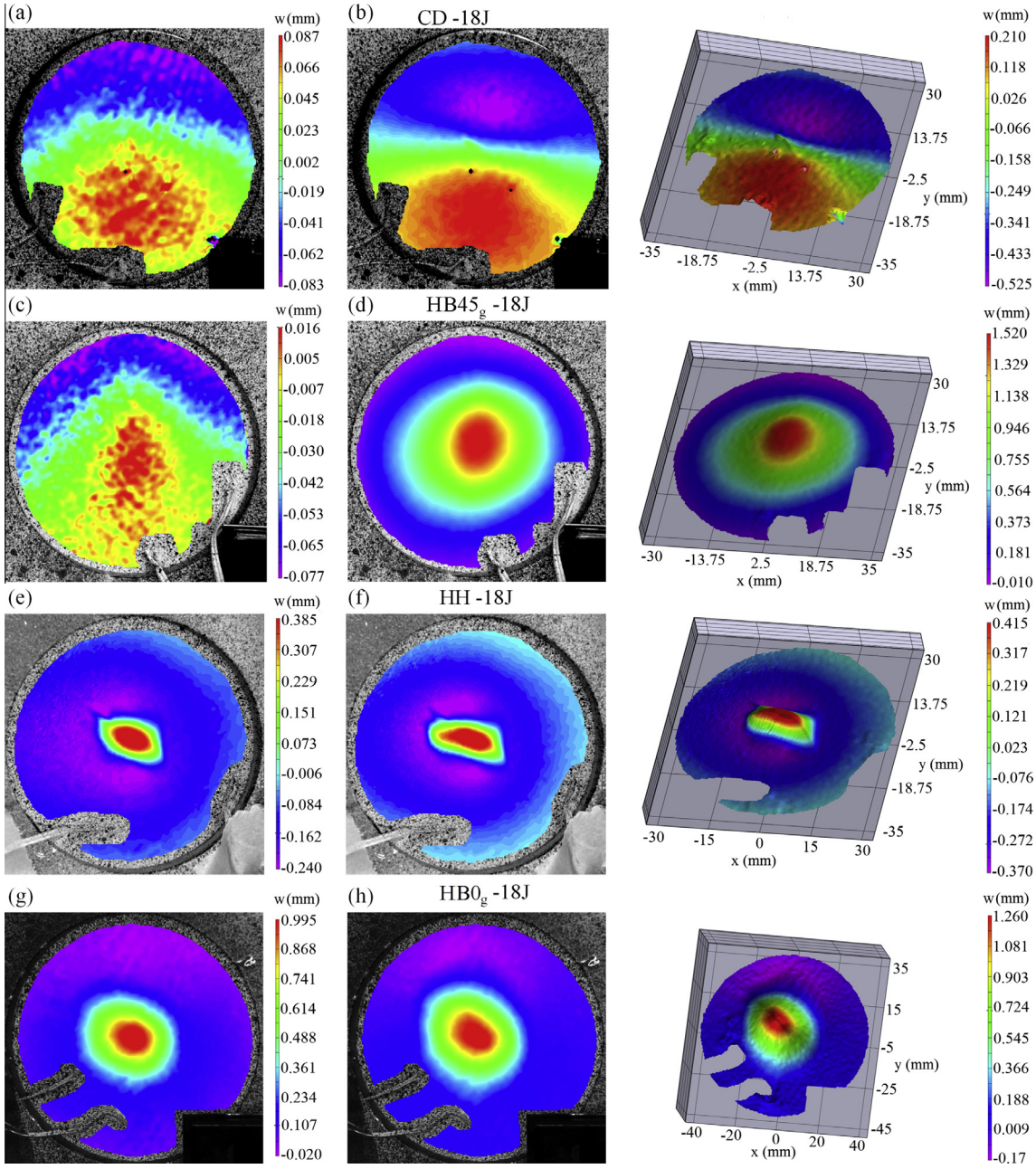

Fig. 6. DIC images during CAI testing with colours indicating out-of-plane displacement from an initial unloaded state. (a) Overall buckling (70 kN) prior to (b) anti-symmetric overall buckling (98 kN) in CD-18Ja. (c) (39 kN) and (d) (137 kN) show evolution of the overall buckling of $HB45_g$-18J. (e) Local buckling above a delamination (93 kN) and (f) following propagation (104 kN) in HH-18J. (g) Local buckling above a delamination (150 kN) and (h) following propagation (155 kN) in $HB0_g$-18J. (For interpretation of the references to colour in this figure legend, the reader is referred to the web version of this article.)

Indeed, failure in the CD-18J followed a change in overall buckling mode shape within the anti-buckling guide, see Fig. 6(a) and (b). The large discontinuities seen on the load vs. strain plot in Fig. 7(a) are co-incident with the sudden jump to a two half-wave buckling anti-symmetric mode from an intermediate asymmetric mode. The mode having developed at loads between those shown in Fig. 6(a) and (b).

A different mode of failure, sublaminate-buckling-driven delamination propagation, was seen in the CD-12J coupon. Similarly, failure of the HH coupons was also caused by propagation of a near-surface delamination following sublaminate buckling see Fig. 6(e) and (f). Propagation is indicated by small discontinuities on the HH-18J load vs. strain plot (in comparison to those in Fig. 7(a)), see circle in Fig. 7(b). In contrast to the $HB0_g$-12J coupon, $HB0_g$-18J failed by sublaminate buckling driven delamination propagation near the interface of the $[0_c/0_g]$ and [±45] blocks as shown by DIC images in Fig. 6(g) and (h). C-scans of $HB0_g$-18J in Fig. 3 indicate delamination propagation occurred at a number of interfaces. Table 3 also shows that damage is more severe and less centrally contained.

The steady divergence of strain gauge curves in Fig. 7(c) and the non-localised, slowly changing pattern of colours in the central region of Fig. 6(e) and (f) are consistent with overall buckling. Material failure induced by (symmetrical) overall buckling caused the failure of all $HB45_g$ coupons and the $HB0_c$-12J and $HB0_g$-12J coupons, see Fig. 6(e) and (f).

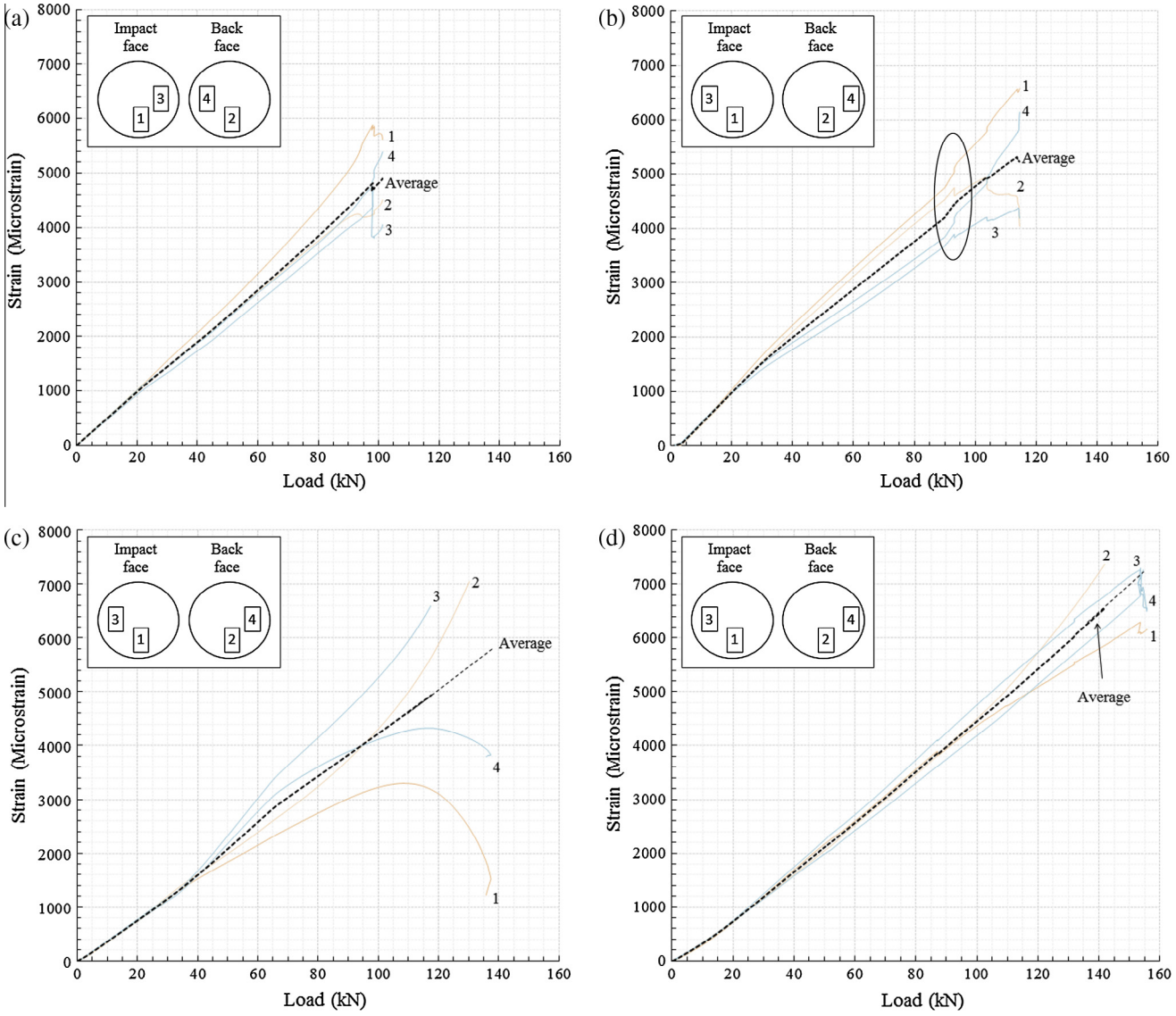

Fig. 7. Load vs. strain plots for compression (CAI) testing of laminates: (a) CD-18Ja, (b) HH-18J, (c) $HB45_g$-18J and (d) $HB0_g$-18J. Discontinuities associated with delamination propagation are highlighted in (b). Insets show the positions of individual strain gauges with relation to Fig. 1. Average strains are extrapolated following strain gauge failure. This is indicated by a reduction in line-thickness of the average strain gauge curve. (For interpretation of the references to colour in this figure legend, the reader is referred to the web version of this article.)

4.3. Discussion of CAI results

Results from the final column of Table 4 show that, for both 12J and 18J impacts, hybrid laminates offer both better structural efficiency and stress to failure than CD laminates for comparable impact energies. The highest difference in performance was for the $HB0_g$-12J coupon in comparison to CD-12J coupon with an increase in failure stress per unit laminate density of 51%. However, a smaller increase of 19% is seen for the $HB45_g$-18J in comparison to the CD-18J coupons. It is likely that suppression of both anti-symmetric overall buckling (see Fig. 6(a) and (b)) and, in the case of the HD laminates, sublaminate-buckling-driven delamination propagation (see Fig. 6(e) and (f)) enables the superior performance of the hybrid laminates. It is believed that the anti-symmetric mode seen in the CD-18J laminates was promoted by through-thickness shear deformation at the centre of the damaged laminate.

This mode is thought to have been driven by intraply cracking in the 90° plies. In contrast, the intact core of 0° plies in the HB laminates prevents the formation of a node line at the point of maximum shear and thus the formation of an asymmetric overall buckling mode. The formation of an anti-symmetric mode promotes shear-driven delamination to a greater extent than a purely symmetric mode. This leads to loss of laminate stability and early failure. Similarly, sub-laminate buckling driven delamination growth ultimately leads to eccentric loading, instability and collapse. The beam-like damage morphology suppresses sublaminate buckling-driven delamination propagation by containing delamination to the core of the laminate.

It is noted that the CD-12J laminate was marginally less structurally efficient than CD-18J coupons. This is believed to be a consequence of the anti-symmetric overall buckling failure of the CD-18J coupons suppressing the formation of the sublaminate buckling driven delamination propagation mechanism seen in the CD-12J coupon.

It is further noted that the load at which overall buckling of the laminate (within the anti-buckling guide window) occurs is dependent on the size of window. However, a significantly smaller window diameter would interfere with local buckling and damage propagation. As all coupons were subject to equal test conditions, and in all cases significant damage was caused and drove failure, failure modes are considered to be consequence of laminate

stacking sequence and impact energy. Hence failure stresses are representative of laminate strength.

5. Discussion

The mechanism for damage formation seen in the $HB45_g$, $HB45_c$, $HB0_c$ and $HB0_g$ coupons meant the majority of the total delamination area was drawn to through-thickness regions near the interface of ply blocks with dissimilar angles (e.g. at the interface of $(\pm 45_c)_4$ and $(0_g/0_c)_4$ blocks), see Table 3 and Fig. 4. A small proportion of the total delamination area was distributed as small delaminations in interfaces near to the impact surface. Such containment of delamination to the centre and near-impact-surface regions of these laminates comes at the cost of individually larger delaminations. Crucially however, little or no delamination occurs in the critical through-thickness region (approximately 20% of laminate thickness from the non-impact face [20], see Table 3) where sublaminate buckling and delamination propagation can occur. Furthermore, the favourable damage morphology of the HB coupons kept the outer sublaminates intact thereby maintaining the bending stiffness of the laminate and delaying overall buckling.

The hybrid laminates were marginally thicker than the CFRP laminates (increasing the second moment of area of the former). However, owing to the lower stiffness of GFRP layers, this does not necessarily result in higher laminate bending stiffnesses (see Table 2). For example laminates $HB45_c$, $HB0_c$ and $HB0_g$ have similar longitudinal and transverse bending stiffnesses to the fully CFRP CD laminates. Hence any full laminate stiffness effects are unlikely to play a role in the difference between delamination sizes and distribution seen in CD and HB laminates.

Some consideration of the results within the context of BVID which is described by dent depth and diameter is required. Low bending stiffness of the HB laminates may produce smaller visible dents following impact. This may hamper impact detection and result in a higher energy impact being required to create BVID than that required for CFRP only laminates. Thus the impact energy comparison used here may be invalidated. However, this argument is degraded by the fact that the some HB coupons failed at a higher stress than the CD-12J coupon despite being subject to 50% higher energy impact.

In summary, although care must be taken regarding differing masses, thicknesses and impact energies when comparing hybrid and CFRP laminates, a comparison of CAI results in Tables 3 and 4 provides the following laminate design principles: (i) separate groupings of angle plies and CFRP/GFRP 0° plies produce favourable damage morphologies and significantly improved CAI strength. (ii) Anti-symmetric overall buckling modes, which caused premature failure of the full CFRP coupons, should be prevented from occurring by removing 90° plies from a laminate whenever secondary load considerations permit. Failure should the only be dependent on maximising global buckling capacity.

6. Conclusions

Experiments conducted in this paper provide benchmark results for comparison of CAI damage tolerance and damage resistance properties of CFRP and CFRP/GFRP hybrid laminates. Hybrid laminates are shown to display increases in structural efficiency of up to 51% for 12J and 41% for 18J impacts in comparison to CFRP laminates with identical impact energies. The extent to which the hybrid laminates outperformed the CFRP laminates in the CAI tests was dependent on the stacking sequence and through-thickness positioning of glass layers. Laminates displaying the highest stresses at failure were those that exploited a structured, imperfection- insensitive, hat-shaped damage morphology to prevent delamination from occurring close to the non-impact surface during impact. The structured morphology preserved both laminate bending stiffness and core ply integrity, thereby inhibiting sublaminate buckling driven delamination propagation and anti-symmetric overall buckling mode failures.

Acknowledgments

The authors are grateful to Agusta-Westland for supply of material and to the University of Bristol for access to their impact test facilities. The first author was supported by the Engineering and Physical Sciences Research Council (Grant No. EP/H025898/1), Airbus Operations and GKN Aerospace. The third author is supported by a Royal Academy of Engineering/GKN Aerospace Research Chair. Data supporting this study are stored by the corresponding author at the University of Bath. Details of how to request access to these data are available from the University of Bath data archive at http://dx.doi.org/10.15125/BATH-00103.

References

[1] Rhead AT, Butler R. Compressive static strength model for impact damaged laminates. Comp Sci Technol 2009;69:2301–7.
[2] Rhead AT, Butler R, Baker N. Analysis and compression testing of laminates optimised for damage tolerance. Appl Compos Mater 2011;18(1):85–100.
[3] Butler R, Rhead AT, Liu W, Kontis N. Compressive strength of delaminated aerospace composites. Philos Trans R Soc Lond A 1965;2012(370):1721–2026.
[4] Jalalvand M, Czel G, Wisnom MR. Numerical modelling of the damage modes in UD thin carbon/glass hybrid laminates. Comp Sci Technol 2014;94:39–47.
[5] Czel G, Wisnom MR. Demonstration of pseudo-ductility in high performance glass/epoxy composites by hybridisation with thin-ply carbon prepreg. Composites Part A 2013;52:23–30.
[6] Yadav SN, Kumar V, Verma SK. Fracture toughness behaviour of carbon fiber epoxy composite with Kevlar reinforced interleave. Mater Sci Eng 2006;132:108–12.
[7] Wardle MW. Impact damage tolerance of composites reinforced with Kevlar aramid fibers. In: Proceedings of ICCM-4 conference, Tokyo; 1982. p. 837–4.
[8] Cantwell WJ, Curtis PT, Morton J. An assessment of the impact performance of CFRP reinforced with high-strain carbon fibres. Comp Sci Technol 1986;25(2):133–48.
[9] Botelho EC, Silva RA, Pardini LC, Rezende MC. A review on the development and properties of continuous fiber/epoxy/aluminum hybrid composites for aircraft structure. Mater Res 2006;9:247–56.
[10] Remmers JCC, de Borst R. Delamination buckling of fibre-metal laminates under compressive and shear loadings. In: Proceedings of 43rd AIAA/ASME/ASCE/AHS/ASC structures, structural dynamics, and materials Con, Denver, Colorado; 2002, AIAA-2002-1730.
[11] Dorey G. Fracture of composites and damage tolerance. J Compos Mater 1975;9(266):61–7.
[12] Dorey G, Sidey GR, Hutchings J. Impact properties of carbon fibre/Kevlar 49 fibre hybrid composites. Composites 1978;9(1):25–32.
[13] Wang W, Makarov G, Shenoi RA. An analytical model for assessing strain rate sensitivity of unidirectional composite laminates. Compos Struct 2005;69:45–54.
[14] Middleton DH, editor, Composite Materials in Aircraft Structures. Singapore: Longman Scientific & Technical; 1990. p. 307.
[15] Kinawy M. Static and fatigue propagation of buckle-driven delaminations under bending and compressive loads. PhD Thesis. Bath, UK: University of Bath; 2011.
[16] Jiang W, Tjong SC, Chu PK, Li RKY, Kim JK, Mai YW. Interlaminar fracture properties of carbon fibre/epoxy matrix composites interleaved with Polyethylene Terephthalate (PET) films. Polym Polym Compos 2001;9(2):141–5.
[17] Lagace PA, Wolf E. Impact damage resistance of several laminated material systems. AIAA J 1995;33(6):1106–13.
[18] Standard test method for measuring the damage resistance of a fiber-reinforced polymer matrix composite to a drop-weight impact event. ASTM Designation: D7136/D7136M-07 2009, http://dx.doi.org/10.1520/D7136_D7136M-07.
[19] Beks F-A. Examination of impact response and damage of composite laminates. The Aeronautical Institute of Sweden (FFA), Rept. FFA TN 1996-29, Bromma, Sweden; 1996.
[20] Melin GL, Schön J. Buckling behaviour and delamination growth in impacted composite specimens under fatigue load: an experimental study. Compos Sci Technol 2001;61:1841–52.